Automated seed detection and three-dimensional reconstruction. I. Seed localization from fluoroscopic images or radiographs

Dragan Tubic
Department of Radiation Oncology, Centre Hospitalier Universitaire de Québec and Centre de Recherche en Cancérologie de l'Université Laval, 11 Côte du Palais, Québec G1R 2J6, Canada and Computer Vision and System Laboratory, Département de Génie Électrique et Genie Informatique, Université Laval, Québec G1K 7P4, Canada

André Zaccarin
Intel Corporation, 2200 Mission College Boulevard, Santa Clara, California 95052-8119

Jean Pouliot
Department of Radiation Oncology, University of California, San Francisco, San Francisco, California 94143-1708

Luc Beaulieu[a)]
Department of Radiation Oncology, Centre Hospitalier Universitaire de Québec and Centre de Recherche en Cancérologie de l'Université Laval, 11 Côte du Palais, Québec G1R 2J6, Canada and Département de Physique, Génie Physique et Optique, Université Laval, Québec G1K 7P4, Canada

An automated procedure for the detection of the position and the orientation of radioactive seeds on fluoroscopic images or scanned radiographs is presented. The extracted positions of seed centers and the orientations are used for three-dimensional reconstruction of permanent prostate implants. The extraction procedure requires several steps: correction of image intensifier distortions, normalization, background removal, automatic threshold selection, thresholding, and finally, moment analysis and classification of the connected components. The algorithm was tested on 75 fluoroscopic images. The results show that, on average, 92% of the seeds are detected automatically. The orientation is found with an error smaller than 5° for 75% of the seeds. The orientation of overlapping seeds (10%) should be considered as an estimate at best. The image processing procedure can also be used for seed or catheter detection in CT images, with minor modifications. © *2001 American Association of Physicists in Medicine.* [DOI: 10.1118/1.1414308]

I. INTRODUCTION

Three-dimensional (3D) reconstruction of implants requires three sets of projections of seeds taken from different perspectives. To provide those projections, the seed centers have to be located on radiographs or fluoroscopic images. Until recently, the seed locations were manually extracted from radiographs. Usually the seeds were marked with opaque paint, which makes a good contrast when scanned. Once the images are obtained, an image processing software can be used to convert the images into binary images and locate seed centers. At our institution, "SCION image" software was used for this purpose. This procedure is, however, very slow and imprecise, since when manually marking more than 100 seeds, the operator is likely to produce errors. Also, positioning of film on the scanner is never perfect.

Automatic seed extraction from fluoroscopic images requires special attention since a simple thresholding will almost never yield an acceptable result, due to the underlying structure that can have both higher and lower intensities than the seeds. To our best knowledge, no algorithm for automatic seed position and orientation extraction from fluoroscopy or radiograph has been presented in the literature.

Recently, CT has become a prominent method for seed localization.[1] However, due to slicing effect of the CT or MRI, it would be very hard, if not impossible, to recover the orientation of the seeds in 3D space. On the other hand, the fluoroscopic images or radiographs represent a projection of the complete seeds, from which the orientation of the seeds can be recovered, as will be shown in the following sections.

This paper describes the procedure that is now clinically used at our institution for automatic seed position extraction including orientations of seeds. The purpose of this procedure is to provide the input for a 3D implant reconstruction algorithm. A companion paper describing a new, robust and precise algorithm for a 3D reconstruction of permanent prostate implants follows up this paper.

The complete procedure of seed extraction from fluoroscopic images requires several steps as shown in Fig. 1. In the sections that follow, each step will be explained in full detail. Some steps are well-known procedures or algorithms and they will be only briefly explained for the sake of completeness.

II. IMAGE ACQUISITION

To provide the input for the implant reconstruction algorithm, we opted for fluoroscopy, which greatly saves acquisition time when compared with radiographs, while reducing costs. Also by using a computer to acquire images, there is no need for radiographs and no manual steps are required
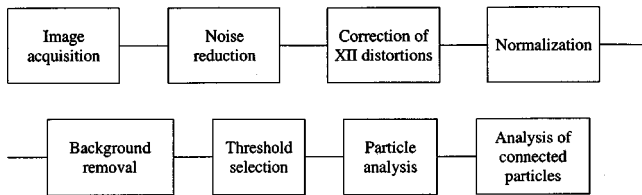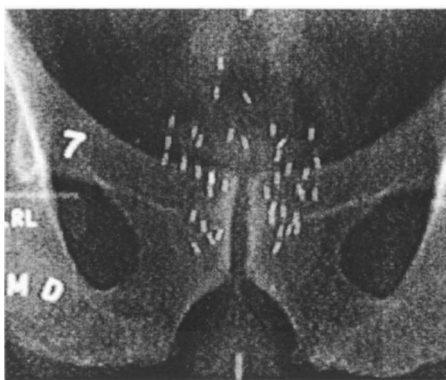
FIG. 1. Seed extraction procedure.

during the acquisition except the positioning of the gantry. However, the procedure presented here can also be used on scanned radiographs.

The algorithm for 3D reconstruction of implants requires three sets of projections of seeds taken from different perspectives. The choice of perspectives is limited by the simulator, which allows only a rotation of the image intensifier and x-ray source around the patient. Also, to avoid imprecision caused by small parallaxes, the difference between the perspectives should be as large as possible, specifically gantry angles of $-45°$, $0°$, and $45°$ would be the best choice. On the other hand, on lateral images the underlying bone structure is too large to allow automatic extraction since the seeds might be almost invisible and masked by noise as seen in Fig. 2(b).

The choice of gantry's angles for the three images is a compromise between the above-explained demands. Empiri-

a)
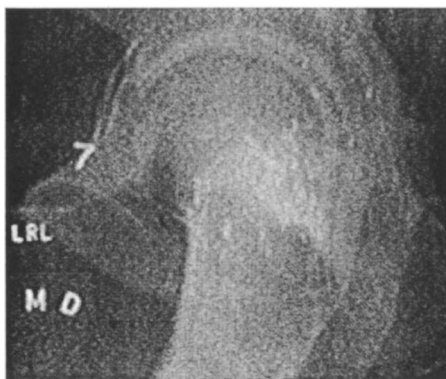
b)

FIG. 2. (a) Image taken at 0°. (b) Image taken at 90°.

cally, we found that the following angles are the optimal choice: image 1—$[-35°, 40°]$; image 2—$0°$; image 3—$[35°, 40°]$.

For most patients, images taken at $±40°$ can be used for automatic seed extraction. However, for larger patients, the underlying bone structure can render these images unusable due to poor contrast and high level of noise. To assure that the reconstruction can be done for all patients, five images (angles $-40°$, $-35°$, $0°$, $35°$, and $40°$) are taken. The image of a seed is only $4×8$ pixel large and the simulator ZOOM option is also used to facilitate seed detection.

III. NOISE REDUCTION AND IMAGE ENHANCEMENT

Since the fluoroscopic images are static, the best way to reduce the noise while preserving all the image features is frame averaging. To improve the noise reduction we should use as many frames as possible. On the other hand, we should avoid irradiating the patient unnecessarily. An image obtained as an average of five frames is a good compromise between image quality and patient exposure (equivalent to one to two radiographs). Note that if a very large number of frames is used for averaging, the resulting image might be blurred due to movement of the patient.

The intensity of x rays at the image intensifier (XII) passing through the patient body is approximately

$$I \propto I_0 \exp\left(-\int_L \mu(x,y)dl\right), \tag{1}$$

where I_0 is initial intensity of x ray, I is the intensity of x rays at the XII, and $\mu(x,y)$ describes the absorption of x rays in the patient body. Clearly, the gray-level intensity of seeds on the image depends on the thickness of other objects (bone structures) through which the x ray travels. To correct this, the image is transformed as follows:

$$v(x,y) = \log(u(x,y)+1), \tag{2}$$

where v is the transformed image, and u is the original image. This way the image becomes a simple sum of the attenuation of the body and the seeds. The contrast of the resulting image is enhanced by normalizing the image using the following transformation:

$$v(x,y) = \frac{u(x,y)-u_{min}}{u_{max}-u_{min}} 255 + 0.5, \tag{3}$$

where u_{min} and u_{max} are minimal and maximal gray levels in the image, v is transformed image, and u is the original image.
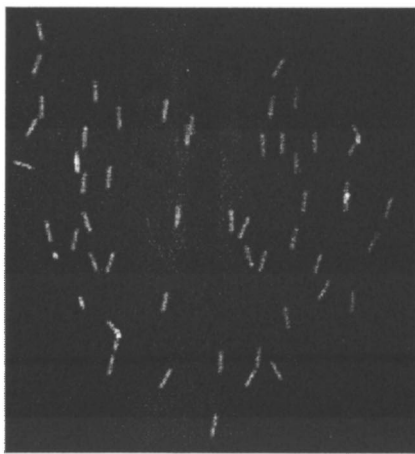
The result of this operation is illustrated in Fig. 3, which shows the original image (a) and the normalized image (b).

IV. CORRECTION OF IMAGE INTENSIFIER DISTORTIONS

For the correction of the XII distortions, the method described in Ref. 2 was adopted. For the sake of completeness it will be briefly described but for more details see Ref. 2.
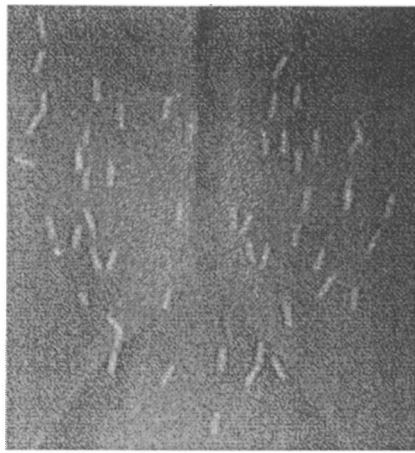
a)

b)

FIG. 3. The original image is shown in (a) while the normalized image appears in (b).

a)

b)

FIG. 4. The calibration grid at (a) 0° and (b) 90°.

The XII distortion is modeled using a fifth-order polynomial. Coefficients of this polynomial are determined using an object of known geometry, usually a rectangular grid of holes as displayed in Fig. 4. The calibration procedure was performed for gantry positions in range −90° to 90°, in 1° steps.
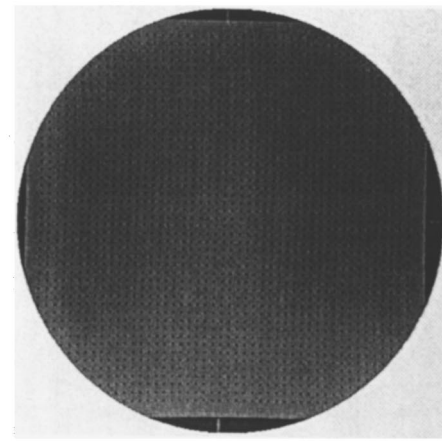
The relation between measured positions of holes and corrected positions can be expressed as follows:

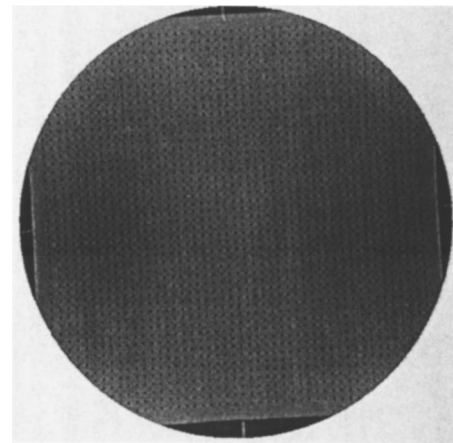$$x_c = \sum_{i=0}^{M} x_m^i \sum_{j=0}^{M} p_{i,j} y_m^j, \tag{4}$$

$$y_c = \sum_{i=0}^{M} y_m^i \sum_{j=0}^{M} q_{i,j} x_m^j, \tag{5}$$

where $M=5$ is the order of the polynomial, x_c, y_c are corrected coordinates, x_m, y_m are measured coordinates, and p, q are polynomial coefficients.

The coefficients are calculated by minimizing the following functions:

$$Sx = \sum_{i=0}^{N} (x_e - x_c)^2, \tag{6}$$

$$Sy = \sum_{i=0}^{N} (y_e - y_c)^2, \tag{7}$$

where x_e, y_e are the correct positions of measured points and N is the number of points. The solution can be obtained using the least-squares technique.

Note that the same procedure that will be described in Sec. V can be used to automatically detect holes on the grid. This way the calibration procedure can be made completely automatic. A software was designed that can detect holes on the grid, find corresponding exact positions, and calculate the polynomial coefficients.

V. BACKGROUND REMOVAL

Before proceeding with seed detection, the image has to be converted to a binary image containing only the seeds. Due to surrounding bone structure, a simple thresholding is not sufficient since the bones can have both smaller and larger intensities than seeds, as shown in Fig. 2(a).

This problem can be effectively solved using a morphological top-hat opening. A description of the mathematical morphology is beyond the scope of this paper and only the operations needed to perform background removal will be presented here. For more details on mathematical morphology see Ref. 3.

In our case, background removal can be done using only four basic operations of mathematical morphology.

Erosion:

$$E(x(m,n)) = \min\{x(m+i,n+j) - k(i,j)\}, \quad i,j \in W. \quad (8)$$

Dilatation:

$$D(x(m,n)) = \max\{x(mi,n-j) + k(i,j)\}, \quad i,j \in W. \quad (9)$$

Opening:

$$D(E(x(m,n))). \quad (10)$$

Closing:

$$E(D(x(m,n))). \quad (11)$$

Here x is an input image, k is a structuring element, and W is its support. The structuring element has a shape of a sphere with radius 7.

Morphological opening can be considered as an operation that cuts peeks smaller than the structuring element. The background removal is performed by subtracting the original image and the opened image. This operation is called top-hat opening. The result of top-hat opening is illustrated in Fig. 5(b).

VI. AUTOMATIC THRESHOLD SELECTION

The intensity of seeds on fluoroscopic images or radiographic films depends on the thickness of bone structures and is different for each patient. It is therefore impossible to specify in advance a fixed threshold. This problem is solved using an algorithm for automatic threshold selection: bidimensional entropy method.[4] This algorithm gives better results than the algorithms based on gray-level histogram only, since it also considers the spatial relationship between pixels.

The underlying principle of this algorithm is the maximization of the entropy of two-dimensional histogram. For each pixel of the original image $u(x,y)$, the average value of its neighborhood (a window 3×3 pixels) is calculated which gives another image $m(x,y)$. The two-dimensional histogram f_{ij} is the number of occurrences of the values i and j in the two images.

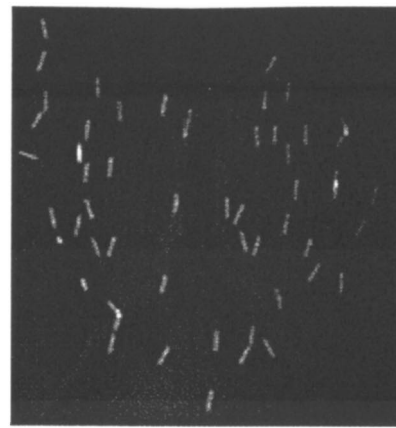Using this histogram we calculate the joint-probability function:

$$p_{ij} = f_{ij}/N,$$

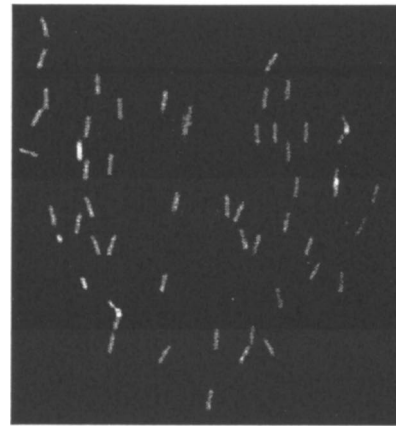where N is the number of pixels in the image.

We assume that the image contains only two groups of pixels: the object (A) and the background (B). The entropy for those two groups of pixels for the thresholds s and t are as follows.
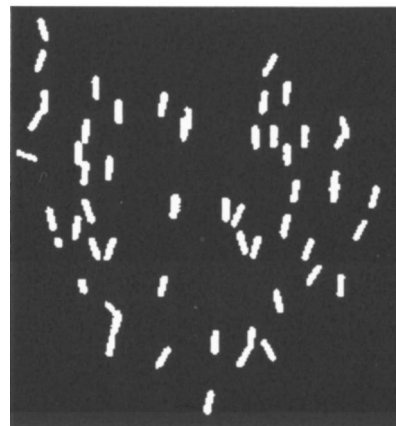
Group A:

$$H(A) = \ln(P_{st}) + H_{st}/P_{st}. \quad (12)$$

a)

b)

c)

FIG. 5. (a) Original image, (b) image after top-hat opening, (c) thresholded image.

Group B:

$$H(B) = \ln(1 - P_{st}) + (H_{mm} - H_{st})/(1 - P_{st}), \quad (13)$$

where

$$P_{st} = -\sum_{i=1}^{s} \sum_{j=1}^{t} p_{ij}, \tag{14}$$

$$H_{st} = -\sum_{i=1}^{s} \sum_{j=1}^{t} p_{ij} \ln(p_{ij}), \tag{15}$$

and m is the maximal gray level.

The threshold values s and t are the values that minimize the following function:

$$\psi(s,t) = \ln[P_{st}(1-P_{st})] + H_{st}/P_{st}$$

$$+ (H_{mm} - H_{st})/(1-P_{st}). \tag{16}$$

Finally the binary image is obtained as follows:

$$b(x,y) = \begin{cases} 1 & \text{if } u(x,y) > s \text{ and } m(x,y) > t \\ 0 & \text{otherwise} \end{cases}. \tag{17}$$

The result of thresholding is shown in Fig. 5.

VII. LABELING

Once the binary image is obtained, all the disconnected components have to be labeled. The simplest algorithm is the recursive labeling, which proceeds as follows:

(1) Starting at the top left-hand corner, scan the image until first *white* pixel is found.
(2) Mark the pixel and test its neighbors (four connected).
(3) For all white pixels repeat step (2) until no more connected pixels remain.
(4) Find the next unlabeled *white* pixel and go to step (2). If the right-bottom corner is reached stop the procedure.

VIII. PARTICLE ANALYSIS

After the labeling, we need to calculate the positions of the seed centers. At this step the problems concerned connected or overlapping seeds. The seeds are separated in two groups: components that contain one seed only and components that contain two or more seeds. In order to achieve this, moments of all components are calculated.[5]

(1) Center of mass:

$$\bar{x} = \frac{1}{N} \sum_{(x,y) \in W} x, \quad \bar{y} = \frac{1}{N} \sum_{(x,y) \in W} y, \tag{18}$$

where W is the region of the component and N is the number of pixels in the component
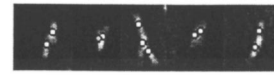
(2) Central moments:

$$\mu_{p,q} = \sum_{(x,y) \in W} (x-\bar{x})^p (y-\bar{y})^q. \tag{19}$$

(3) Orientation:

$$\theta = \frac{1}{2} \tan^{-1} \left[\frac{2\mu_{1,1}}{\mu_{2,0} - \mu_{0,2}} \right]. \tag{20}$$

(4) Bounding rectangle (smallest rectangle containing the particle).

a)

b)

FIG. 6. (a) Examples of overlapping seeds. (b) Ideal seeds at various angles.

To obtain the vertices of this rectangle, the pixels belonging to the particle are transformed as follows:

$$\alpha = x \cos\theta + y \sin\theta, \tag{21}$$

$$\beta = -x \sin\theta + y \cos\theta, \tag{22}$$

$\alpha_{\min}$, $\alpha_{\max}$, $\beta_{\min}$, and $\beta_{\max}$ are vertices of the rectangle: $(\alpha_{\min}, \beta_{\min})$, $(\alpha_{\min}, \beta_{\max})$, $(\alpha_{\max}, \beta_{\min})$, and $(\alpha_{\max}, \beta_{\max})$.

Length of the component:

$$l = \alpha_{\max} - \alpha_{\min}. \tag{23}$$

Width of the component:

$$w = \beta_{\max} - \beta_{\min}. \tag{24}$$

(5) Area, simply defined as the number of pixels.

Finally using the above-presented analysis, the components are classified as follows:

(1) Components whose area is smaller than 12 are considered as noise and are ignored.
(2) Components whose length l and width w satisfy $l < 15$, and $w < 7$ are considered as single seed.
(3) The other components contain more than one seed and are analyzed separately.

For the components that contain one seed only, its center is taken to be the center of mass. $(\bar{x}, \bar{y})$.

The other components contain more than one seed. A few cases of overlapping seeds are illustrated in Fig. 6(a). Those components are analyzed using an algorithm based on simulated annealing. In essence the algorithm tries to reconstruct the component using the predefined "perfect" seeds, Fig. 6(b). In other words the algorithm tries to find the number, positions, and the orientations of the "perfect" seeds that best approximates the original particle by minimizing the following cost function:

$$\sum_{(x,y) \in W} |u(x,y) - r(x,y)|, \tag{25}$$

where u is defined as $u(x,y) = o(x,y) * b(x,y)$. Images b and o are the binary image and the image after the morphological opening, respectively, while $r(x,y)$ is reconstructed image:

a)
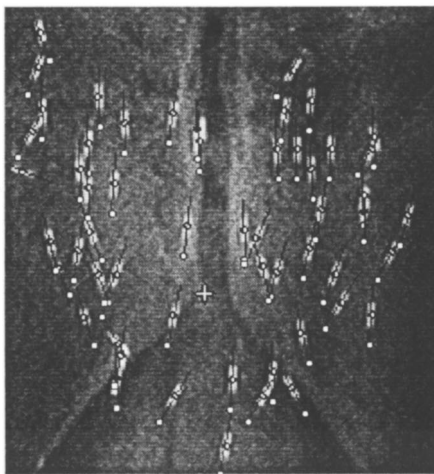
b)

FIG. 7. (a) Automatically detected seeds as found by the algorithm. (b) Automatic evaluation of the seed orientations based on the moment analysis of the particles.

$$r(x,y) = \sum_{i=1}^{N} S_{\varphi_i}(x+x_i, y+y_i). \tag{26}$$

$S_{\varphi_i}(x,y)$ is an image of "ideal" seed with an orientation φ_i and (x_i, y_i) is the position of its center. The average intensity of the "ideal" seed is adjusted to correspond to the average intensity of the particle. The solutions of the problem are the positions (x_i, y_i), the orientations φ_i, and number of seeds N that minimizes the function Eq. (25).

The function [Eq. (25)] is minimized using simulated annealing.[6,7] The parameters of the algorithm are specified as follows:

(i)　The initial configuration is random.
(ii)　L_k is fixed. Steps (2) and (3) are repeated until the number of accepted reconfigurations is larger or equal to 10× number of seeds or the number of rejected reconfigurations is larger than 100× number of seeds.
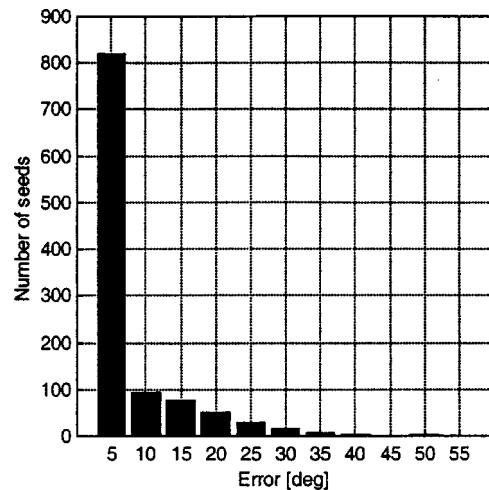
FIG. 8. Determination of the uncertainty of the seed orientation found by the algorithm for 2000 individually identified seeds. The error is computed by subtraction between the real seed orientation as manually measured (precision not better than 5°) and the one automatically found.

(iii)　The "temperature" is lowered using the following schedule: $c_{k+1} = c_k \cdot 0.99$.
(iv)　The algorithm stops when the temperature falls below 0.5.

The reconfiguration is made as follows.

Choose at random a pixel inside the particle, one seed, and the new orientation for the seed. If the position is occupied, exchange the positions of the chosen seed and the seed that occupies the chosen position. If not, assign a new position and orientation to the chosen seed.

Since the number of seeds in the particle is unknown the algorithm is repeated for the clusters of 2 and 3. The probability that the particle contains more than three seeds is very small, and if it happens manual intervention is usually required. The number of seeds that minimizes the cost function is accepted as the correct number of seeds.

IX. RESULTS AND CONCLUSIONS

The algorithm has been tested on 75 images and used clinically on more than 300 images. On average the algorithm detects about 92% of the seeds correctly. An example of the extraction procedure is shown in Fig. 7(a). The automatically estimated orientations, for a sample of 2000 seeds from clinical implants, were compared with manually estimated orientations. The histogram in Fig. 8 shows the error distribution of the orientation estimate. An example of the orientation estimation is shown in Fig. 7(b).

The complete procedure described previously is implemented in C++. On average, the execution time of the algorithm was 16 s/image. The first three steps do not depend on the number of seeds and the execution time for those steps was approximately 1 s. The execution time for the component analysis is negligible. Analysis of components that contain overlapping seeds requires about 15 s. All results were obtained using a PC with Intel Pentium III processor running at 733 MHz.
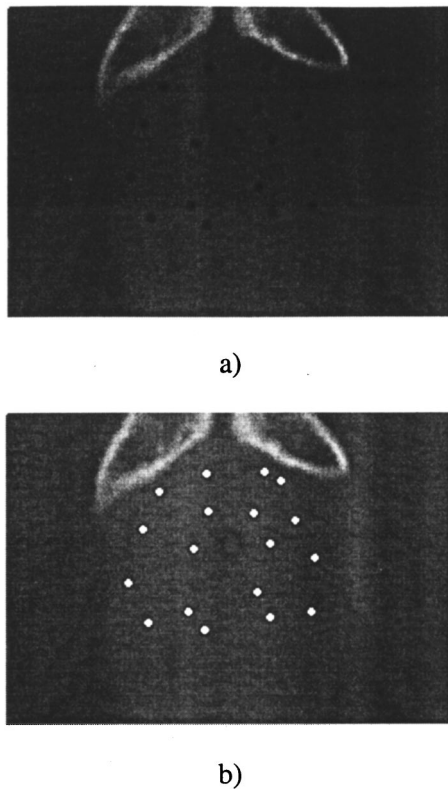
a)

b)

FIG. 9. Illustration of the detection of the seeds in CT images. (a) Original image. (b) Detected seeds.

a)

b)

FIG. 10. Illustration of the detection of the catheters in CT images. (a) Original image. (b) Detected catheters.

Radioactive seeds and catheters can be extracted from CT images using the same image processing procedure. As shown in Fig. 9, the algorithm correctly detects the seeds, but can also produce false seeds near the edges of bones. For catheters, the image depicted in Fig. 10(a) can be inverted and the problem becomes similar to the seed detection problem. The detected holes are shown in Fig. 10(b). The advantage of this type of detection is that the image processing is performed automatically without user selected thresholds. The user does not need to have any prior knowledge about gray levels or CT numbers. However, an additional step is required to remove false detection near edges of bones. That modification is beyond the scope of this paper and will be described elsewhere.

In conclusion, we have developed an automatic and fast seed localization algorithm that operates both on fluoroscopic images or digitized radiographs.

Results are better on fluoroscopic images probably because of the frame averaging used for this modality. Furthermore fluoroscopy is now more commonly available in the operating room, which makes this algorithm highly useful for intraoperative purposes.
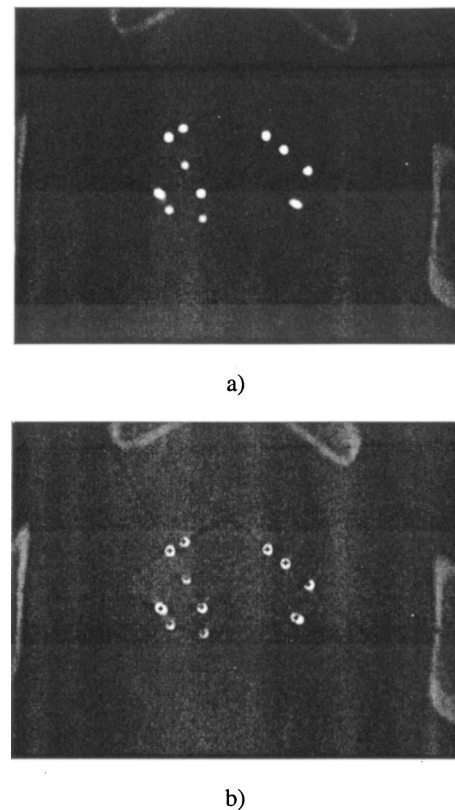
ACKNOWLEDGMENTS

[a] Electronic mail: beaulieu@phy.ulaval.ca

[1] D. H. Brinkmann and R. W. Kline, "Automated seed localisation from CT datasets of the prostate," Med. Phys. **25**, 1667–1672 (1998).

[2] D. P. Chakraborty, "Image intensifier distortion correction," Med. Phys. **14**, 249–252 (1987).

[3] R. M. Haralick, S. R. Sternberg, and X. Zhuang, "Image analysis using mathematical morphology," IEEE Trans. Pattern Anal. Mach. Intell. **PAMI-9**(3), (1987).

[4] A. S. Abutaleb, "Automatic thresholding of grey-level pictures using two-dimensional entropy," Comput. Vis. Graph. Image Process. **47**, 22–32 (1989).

[5] A. K. Jain, *Fundamentals of Digital Image Processing* (Prentice–Hall, Englewood Cliffs, NJ, 1989).

[6] S. Kirkpatrick, C. D. Gellat Jr., and M. P. Vecchi, "Optimisation by simulated annealing," Science **220**, 671–680 (1982).

[7] E. Aarts and J. Korst, *Simulated Annealing and Boltzmann Machines* (Wiley, New York, 1989).